JES Focus Issue of Selected Papers from IMLB 2018

(De)Lithiation Mechanism of Hierarchically Layered $LiNi_{1/3}Co_{1/3}Mn_{1/3}O_2$ Cathodes during High-Voltage Cycling

Weibo Hua,[1,z] Björn Schwarz,[1,z] Michael Knapp,[1,2] Anatoliy Senyshyn,[3] Alkesandr Missiul,[4] Xiaoke Mu,[5] Suning Wang,[6] Christian Kübel,[2,5,7] Joachim R. Binder,[1] Sylvio Indris,[1,2,z] and Helmut Ehrenberg[1,2,8,*]

[1]*Institute for Applied Materials (IAM), Karlsruhe Institute of Technology (KIT), 76344 Eggenstein-Leopoldshafen, Germany*
[2]*Helmholtz Institute Ulm for Electrochemical Energy Storage (HIU), Karlsruhe Institute of Technology (KIT), 76344 Eggenstein-Leopoldshafen, Germany*
[3]*Heinz Maier-Leibnitz Zentrum, Technische Universität München, D-85747 Garching, Germany*
[4]*CELLS-ALBA Synchrotron, Cerdanyola del Valles, E-08290 Barcelona, Spain*
[5]*Institute of Nanotechnology (INT), Karlsruhe Institute of Technology (KIT), 76344 Eggenstein-Leopoldshafen, Germany*
[6]*College of Chemical Engineering, Sichuan University, Chengdu, 610065, People's Republic of China*
[7]*Karlsruhe Nano Micro Facility (KNMF), Karlsruhe Institute of Technology (KIT), 76344 Eggenstein-Leopoldshafen, Germany*
[8]*Technische Universität Darmstadt, Department of Geo- and Material Science, 64287 Darmstadt, Germany*

In view of the requirements for high-energy lithium ion batteries (LIBs), hierarchically layered $LiNi_{1/3}Co_{1/3}Mn_{1/3}O_2$ (NCM111) cathode materials have been prepared using a hydroxide coprecipitation method and subsequent high-temperature solid-state reaction. The diffraction results show that the synthesized NCM111 has a well-defined layered hexagonal structure. The initial specific discharge capacity of a Li/NCM111 cell is 204.5 mAh g^{-1} at a current density of 28 mA g^{-1} between 2.7 and 4.8 V. However, the cell suffers from poor capacity retention over extended charge-discharge cycles. The structural evolution of NCM111 electrode during electrochemical cycling is carefully investigated by in situ high-resolution synchrotron radiation diffraction. It is found that the nanodomain formation of a layered hexagonal phase H3 and a cubic spinel phase after charging to voltages above 4.6 V is the main source for the structural collapse in *c* direction and the poor cycling performance. This process is accompanied by the removal of oxygen, the transition metal (TM) migration and the crack generation in the nanodomains of the primary particles. These results may help to better understand the structural degradation of layered cathodes in order to develop high energy density LIBs.
 [DOI: 10.1149/2.0051903jes]

Manuscript submitted September 14, 2018; revised manuscript received October 16, 2018. Published November 6, 2018. *This paper is part of the JES Focus Issue of Selected Papers from IMLB 2018.*

In recent years lithium-ion batteries (LIBs) have drawn considerable attention due to their potential application in large-scale energy storage systems (ESS) and electric vehicles (EVs).[1–3] Layered $LiNi_{1/3}Co_{1/3}Mn_{1/3}O_2$ (NCM111) cathode material is particularly attractive because of its high thermal stability, high volumetric energy density, and low cost.[4–6] When NCM111 is employed as a cathode material in LIBs, its specific energy (E_S) is the result of the discharge potential (V) and the specific capacity (C) ($E_S = \int C(V)dV$, where $C(V)$ is the discharge capacity as a function of voltage).[7–9] In theory, the specific capacity is the amount of charge (electrons or lithium ions) that participated in the electrochemical redox reaction per formula unit.[10,11] Making a higher capacity of the NCM111 cathode viable requires extraction/insertion of a larger amount of lithium ions from/into the host structure by an increased potential window, with the concomitant addition or removal of electrons. When more lithium ions are extracted from the NCM111 host structure (i.e. $x > 0.6$ in $Li_{1-x}Ni_{1/3}Co_{1/3}Mn_{1/3}O_2$ corresponding to a specific discharge capacity beyond $\sim$ 160 mAh g^{-1}), however, the layered structure will be considerably damaged by oxygen release.[8,12]

To improve the cycling stability of NCM111 at high cutoff voltages, tremendous efforts have been undertaken on morphological control,[7,13–15] because the shape and particle size of the active materials can significantly affect the reaction mechanism during cycling. For Li-rich materials, having a layered structure with similarity to NCM111, Dahn et al.[16] proposed a surface/bulk two-phase reaction mechanism depending on the inner particle Li-diffusion path lengths. Only for very small particles (less than 1 μm), a single-phase reaction mechanism can be rationally expected. Shu et al.[17] reported that the structural transition from a layered hexagonal H1 phase to a H2 phase and finally to a H3 phase was observed in a spherical $LiNi_{0.5}Co_{0.2}Mn_{0.3}O_2$ (NCM523) cathode with large particle size (> 10 μm) in the range from 2.0 to 4.9 V, with the H3 phase showing very poor structural stability during electrochemical cycling. Recently, our group demonstrated that NCM111 with a small particle size (200 $\sim$ 400 nm) can provide excellent structural reversibility by suppressing the H3 phase when charged up to 4.8 V.[8]

With a three-dimensional (3D) hierarchical architecture, the NCM111 cathode has been found to present a good cycling performance in LIBs because the small primary particles are beneficial for ionic and electronic mass transport while the agglomerated particles can contribute to a good mechanical integrity and structural stability.[6,14,18] An interesting question that needs to be addressed is whether the (de)lithiation mechanism of hierarchically layered NCM111 is a surface-bulk-limited reaction (two-phase reaction) or surface-limited redox reaction (single-phase reaction) during high voltage cycling. In the present study, NCM111 agglomerates were prepared by a hydroxide coprecipitation reaction and subsequent high temperature lithiation process. The electrochemical behavior of the assembled Li/NCM111 cell was investigated in the voltage range between 2.0 and 4.8 V. In situ synchrotron radiation diffraction measurements were performed on the prepared Li/NCM111 cell to trace the structural evolution of the NCM111 electrode during the high voltage charge-discharge.

Experimental

Preparation of NCM111.—The synthesis procedure of $LiNi_{1/3}Co_{1/3}Mn_{1/3}O_2$ (NCM111) has been described in detail before.[6,7,19,20] The transition metal hydroxide precursor

*Electrochemical Society Member.
[z]E-mail: weibo.hua@partner.kit.edu; bjoern.schwarz@kit.edu; sylvio.indris@kit.edu

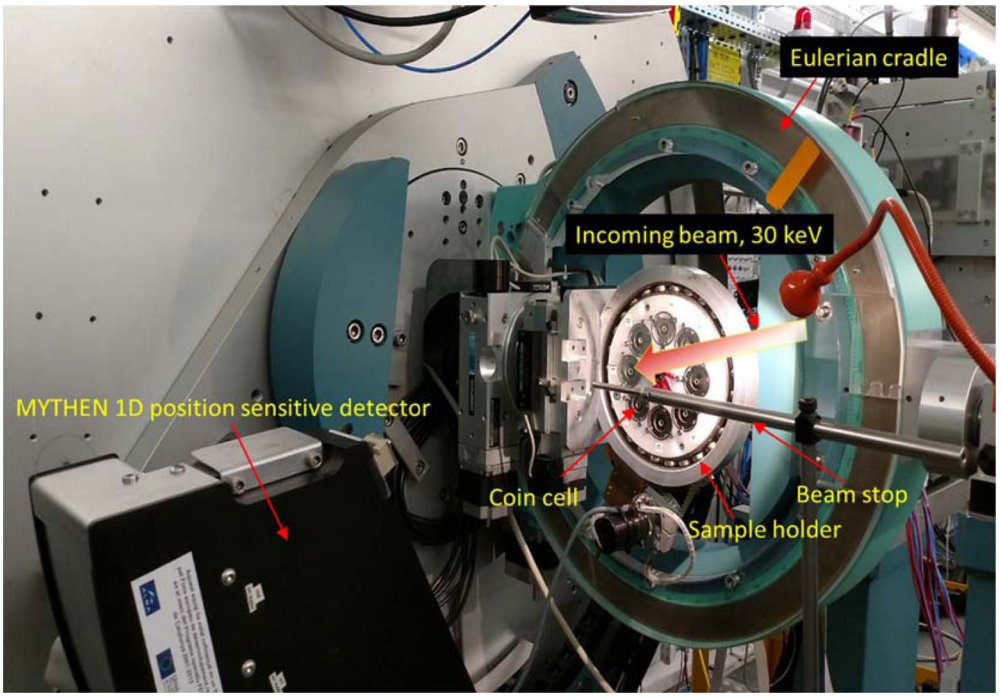

Figure 1. Custom-made sample holder for in situ SRD studies on Li ion batteries, during operation, at MSPD beamline.

$Ni_{1/3}Co_{1/3}Mn_{1/3}(OH)_2$ was prepared via a hydroxide coprecipitation process in a continuously stirred tank reactor (CSTR). An aqueous solution of $NiSO_4 \cdot 6H_2O$, $CoSO_4 \cdot 7H_2O$ and $MnSO_4 \cdot H_2O$ was prepared with Ni:Co:Mn molar ratio of 1:1:1. Sodium hydroxide solution was pumped into the reactor under pH control. The coprecipitation reaction proceeded with the addition of 5 M NH_3(aq) solution at 0.15 ml min^{-1} and 2 M transition metal sulfates solution at 1 ml min^{-1}. During the reaction process, the concentration, pH value, temperature, and stirring speed were carefully controlled and adjusted. The resulting precipitates were dried at 110°C for 12 h in air, and then thoroughly mixed with lithium carbonate. The NCM111 powders were synthesized by calcining the mixture of precipitates and Li_2CO_3 initially at 550°C for 6 h and then at 850°C for 12 h in air.

Material characterization.—The crystallographic structure of the layered NCM111 was characterized by high-resolution synchrotron radiation diffraction (SRD) and high-resolution neutron powder diffraction (NPD), which were performed at the beamline MSPD at ALBA (Barcelona, Spain) and beamline SPODI at MLZ (Garching, Germany), respectively. The unit cell parameters of NCM111 were refined simutaneously to the SRD and NPD patterns using the Fullprof software. The shape and particle size of the sample were examined by a Merlin scanning electron microscope (SEM, Zeiss, Oberkochen) operated with an accelerating voltage of 10 kV. The structure of the material was also investigated by high-resolution transmission electron microscopy (HRTEM) and selected area electron diffraction (SAED) measurements performed using a FEI Titan 80–300 (FEI Compnay, Portland). The local structure of the specimen was probed by Raman spectroscopy (Horiba Scientific, Lille). In situ SRD experiments were performed at the beamline MSPD at ALBA, see Figure 1, using synchrotron radiation with an energy of 30 keV ($\lambda = 0.41287$ Å) and an exposure time of 60 seconds per pattern. The diffraction patterns were collected using a MYTHEN 1D position sensitive detector. For in situ diffraction measurements, CR2025 coin cells with glass windows (diameter = 5 mm) were used.

Electrochemical tests.—Electrochemical tests were performed on a coin-type half-cell (CR2032) composed of a cathode, a lithium metal anode, a porous polypropylene membrane (Celgard 2323) as the separator, and a LP30 electrolyte. The cathode was fabricated by mixing the NCM111 active material, super P carbon (electrical conductor), and polyvinylidene fluoride (PVdF) binder in a mass ratio of 80:13:7. Liquid LP30 electrolyte was 1 M $LiPF_6$ solution in the solvents of 1:1 (w/w) ethylene carbonate (EC) and dimethyl carbonate (DMC). The coin cells were tested at a current density of 0.1 C (1 C = 280 mA g^{-1}) between 2.7 and 4.8 V (versus Li/Li^+).

Results and Discussion

The surface morphology of as-prepared precursor and NCM111 is displayed in Figure 2. The SEM image, Figure 2a, shows that the as-synthesized precursor is composed of many flower-like secondary crystalline grains with a particle size around 3 μm. These secondary particles consist of many ultra-thin nano-plates to form a kind of rose flower hierarchical architecture. After the high-temperature lithiation reaction, the mixture of precursor and lithium source converts into the lithium insertion compound, i.e. $LiNi_{1/3}Co_{1/3}Mn_{1/3}O_2$ (NCM111). The SEM image of NCM111 demonstrates that the as-prepared final product reveals secondary particles agglomerated from packed primary nanosheets or polyhedra, see Figure 2b.

Since neutron powder diffraction is a powerful tool to probe the low-Z elements such as lithium and to distinguish between Ni, Co and Mn, high-resolution synchrotron radiation powder diffaction (SRD) and high-resolution neutron powder diffraction (NPD) were combined to obtain accurate structure information of the synthesized NCM111. All the reflections on the SRD and NPD patterns of NCM111 can be indexed according to a typical hexagonal layered structure with the space group of $R\bar{3}$m while no impurity reflection is detected. Figure 3 shows the Rietveld co-refinement results on SRD and NPD patterns. The co-refinements were performed by using a single α-$NaFeO_2$ layered structure model where Li and transition metals (TMs) are mainly located on 3*b* site and 3*a* site, respectively, and oxygen is positioned on 6*c* site. The structure is then refined simultaneously against both data sets, SRD and NPD diffraction data, with a single structural model with constrained structural parameters.[21] Hence, simultaneous analysis of SRD and NPD helps to obtain an accurate crystal structure of these Li insertion compounds. The good fit proves the proposed layered model to be correct. The obtained lattice parameters

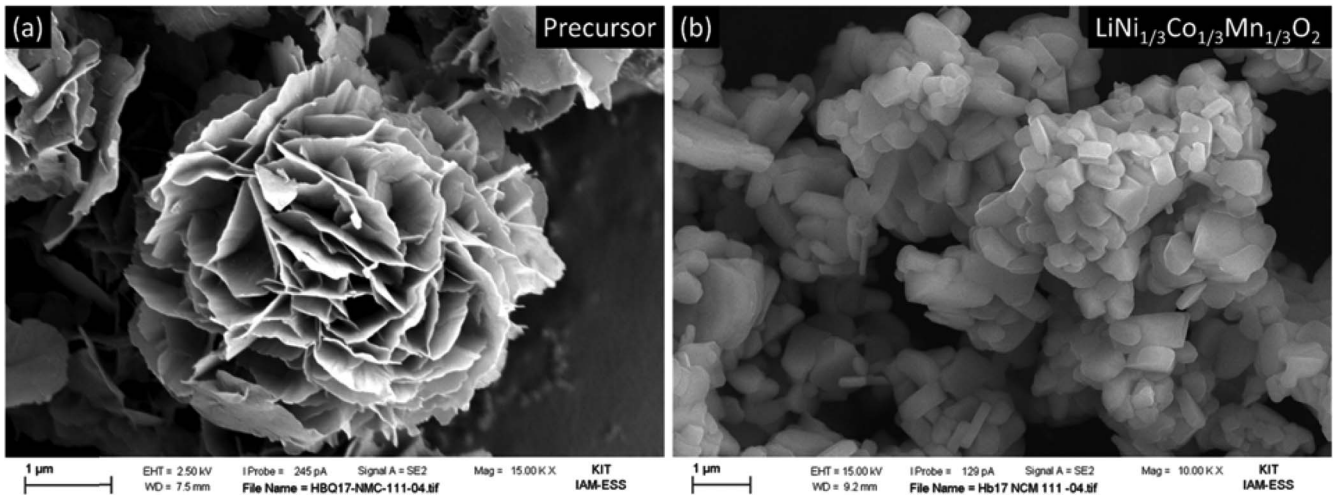

Figure 2. SEM images of (a) precursor and (b) NCM111.

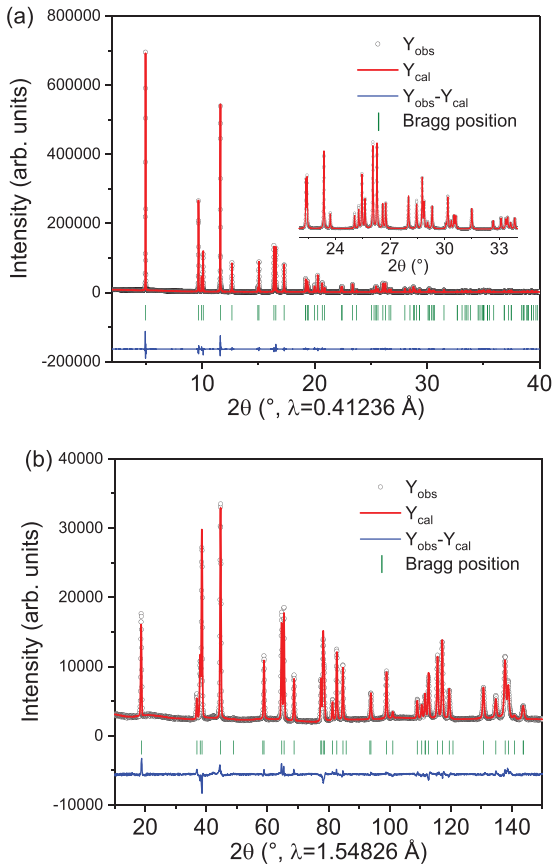

Figure 3. Simultaneous Rietveld refinement on a) SRD and b) NPD patterns of NCM111.

(e.g., *a*, *c* and *c*/*a*) of NCM111 listed in Table I are very close to those previously reported in References 22 and 23. The layered rhombohedral phase can be considered as a cubic rock-salt/spinel derivative, in which all these three structures have a similar cubic-close packed (ccp) oxygen lattice.[24] The oxygen sub lattice of the layered phase is deemed to be distorted from the face-centered cubic (fcc) array in the projection of the hexagonal *c* axis. Such distortion results in a splitting of the reflections that are assigned to 006/102 and 018/110 in the SRD and NPD patterns. The parameter *c*/*a* ratio is an important indication for the distortion from the cubic phase. When the distortion

Table I. Lattice parameters and crystallographic information of NCM111 obtained from the simultaneous refinement against the SRD and NPD data.

Cell parameters

Space group: $R\bar{3}m$, $a = 2.864$ Å, $c = 14.257$ Å, $c/a = 4.977$, $V = 101.309$ Å^3, Atomic positions

Name	site	*x*	*y*	*z*	B_{iso}	Fract
Li1	3*a*	0	0	0	1.086	0.967
Ni2	3*a*	0	0	0	1.086	0.046
Ni1	3*b*	0	0	$\frac{1}{2}$	0.131	0.288
Li2	3*b*	0	0	$\frac{1}{2}$	0.131	0.033
Co1	3*b*	0	0	$\frac{1}{2}$	0.131	0.333
Mn1	3*b*	0	0	$\frac{1}{2}$	0.131	0.333
O1	6*c*	0	0	0.241	0.524	1.000

Refinement parameters

Constraints:
$B_{iso}(Ni1) = B_{iso}(Co1) = B_{iso}(Mn1) = B_{iso}(Li2)$; $B_{iso}(Li1) = B_{iso}(Ni2)$;
Fract (Ni1) + Fract (Ni2) = 0.333; Fract (Li1) + Fract (Li2) = 1.000
$R_{wp} = 10.8\%$, $R_p = 9.06\%$, χ^2: 25.25 for SRD
$R_{wp} = 10.0\%$, $R_p = 12.8\%$, χ^2: 5.26 for NPD

Note: B_{iso} is the thermal displacement parameter; Fract is the fractional occupancy of the atom on this site; the occupation of Co1, Mn1 and O1 was fixed accoring to the stoichiometry. An equivalent description of the crystal structure can be given with an O1 *z* parameter >0.25, Li on the 3*b*, and the transition metals on the 3*a* site.

along the *c* direction is absent, the *c*/*a* ratio is equivalent to $\sqrt{24} = 4.899$, and the two split reflections of 006/102 and 018/110 would merge into single reflections.[6,25] As shown in Figure 3 and Table I, the reflections split 006/102 and 018/110 doublets are clearly observed in both, SRD and NPD patterns, and the *c*/*a* ratio of NCM111 is higher than $\sqrt{24}$, evidencing a well-crystalline α-$NaFeO_2$ layered structure in the synthesized NCM111 sample. Generally, the divalent nickel could easily enter into the lithium layer in the layered phase due to the comparable radius of Li^+ and Ni^{2+} ions ($r_{Li^+} = 0.76$ Å, $r_{Ni^{2+}} = 0.69$ Å).[20] The cation mixing can induce the formation of a rock-salt phase that weakens the intensity of the 003 reflection in the SRD pattern but has no influence on the 104 reflection.[20,26] Therefore, the integrated intensity ratio of the 003 to 104 reflections (I_{003}/I_{104}) can be regarded as an evaluation of the cation disorder in the layered structure. The co-refinement results show that the content of Ni in the Li layer is approximately 4.6%, which is in good agreement with the values given in the literature for NCM111.[25,27]

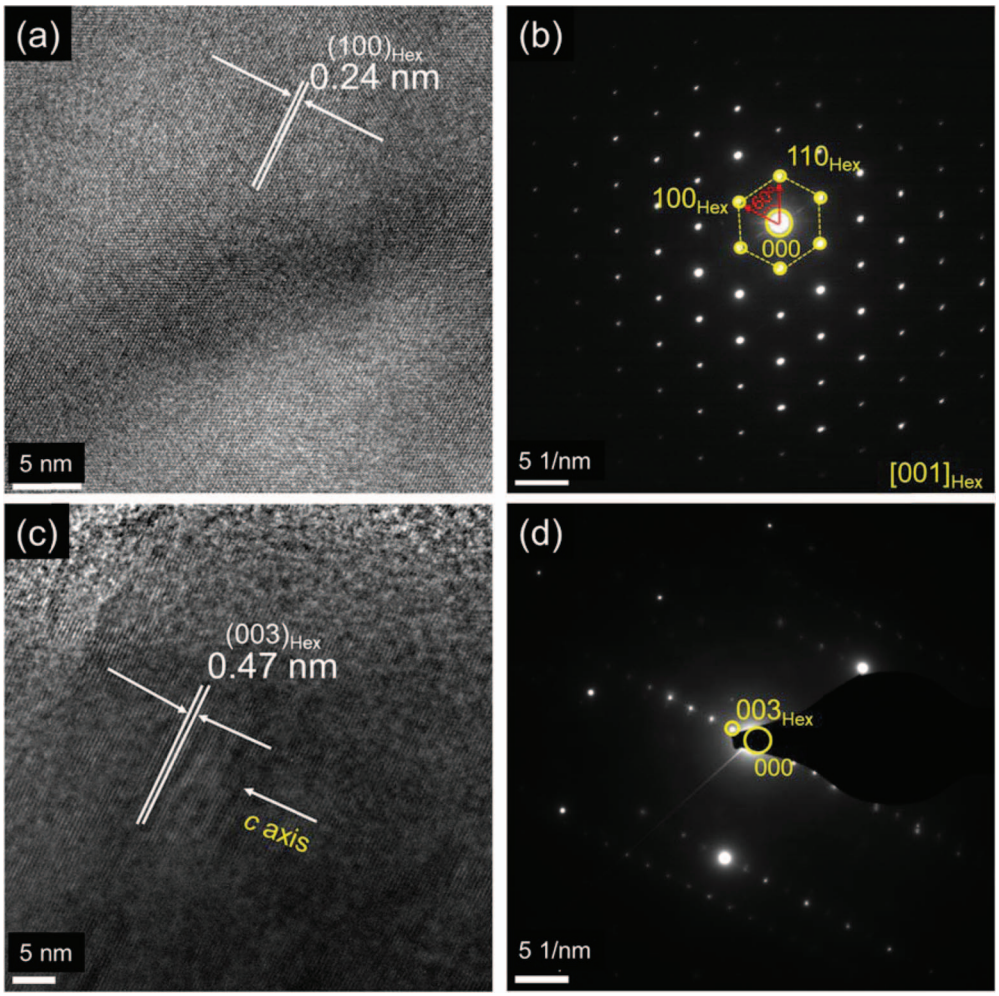

Figure 4. (a) HRTEM image and (b) its corresponding SAED pattern of the NCM111 from a $[001]_{Hex}$ projection; (c) HRTEM image and (d) the corresponding SAED pattern of the NCM111 from a $[010]_{Hex}$ direction. Hex denotes hexagonal phase H1.

High-resolution transmission electron microscopy (HRTEM) and selected area electron diffraction (SAED) were used to further investigate the crystal structure for a few selected grains. The HRTEM image of the as-prepared NCM111 in Figure 4a reveals lattice fringes with interplanar distances of 2.4 Å that can be ascribed to the (100) plane of the hexagonal NCM111 phase. The corresponding SAED pattern in Figure 4b can be indexed as $[001]_{Hex}$ projection, revealing that these particles are single-crystalline with a hexagonal symmetry. Figure 4c exhibits a HRTEM image along the other zone axis orientation of the as prepared NCM111. The HRTEM image shows lattice spacing with distances of 4.7 Å, in good agreement with the *d*-value of the (003) plane of typical layered $LiNi_{1/3}Co_{1/3}Mn_{1/3}O_2$. The SAED pattern (Figure 4d) fits well to layered NCM111 close to $[010]_{Hex}$ orientation, a symmetry that cannot be generated by a cubic phase, further confirming a layered structrure in the synthesized NCM111.

In order to investigate the electrochemical properties of the prepared NCM111 agglomerate in LIBs during high voltage cycling, the fabricated coin-type half cells (CR2032) were cycled in the voltage range of 2.7–4.8 V using a current density of 28 mA g^{-1} (0.1 C) at room temperature. Figure 5a shows the continuous cycling performance of the Li/NCM111 cell and the corresponding coulombic efficiency. As observed in Figure 5b, the NCM111 cathode undergoes a drastic reversible capacity drop with increasing number of cycles. With $\sim$ 51% of the initial capacity, the discharge capacity of the Li/NCM111 cell after 73 cycles is 104.9 mAh g^{-1}, which is close to the value reported in literature.[28–31] The corresponding charge-discharge curves of the Li/NCM111 half cell are displayed in Figure 5b. The discharge capacity of the NCM111 electrode gradually decreases and the cell polarization successively increases during the Li intercalation and deintercalation, suggesting a severe structure degradation because of a considerable amount of Li insertion into or extraction from the NCM111 host matrix. In addition, the high overpotential is observed at the end-stage cycling, which is probably caused by the crack formation on the NCM111 agglomerates that could induce the generation of new solid electrolyte interface (SEI) membranes on the interfaces between the contracted primary particles and/or in the nanodomain of the primary particles.

To figure out the reasons why the NCM111 delivers a poor electrochemical cycling performance between 2.7 and 4.8 V, in situ high-resolution synchrotron radiation diffraction was performed. In order to clearly illustrate the phase transition, the contour plots of the reflection intensity and position for several main reflections as a function of reaction time during the first cycle are exhibited in Figure 6. All reflections in the in situ SRD patterns of NCM111 can be indexed to a layered structure with the $R\bar{3}m$ space group, except for strong reflections at $\sim$ 11.7° and $\sim$ 16.6°, which originate from the Al current collector. It should be mentioned that the 003, 104, 018 reflections mainly represent the evolution of the average metal-metal inter-slab distance of the layered structure (i.e. *c* lattice parameter), while 101, 110 reflections mostly reflect the change in the average metal-metal intra-slab distance of the layered phase (i.e. *a* or *b* lattice constant). Between the open-circuit voltage and 4.2 V, the 003, 104, 018 reflections shift toward lower scattering angles while 101, 110 reflections

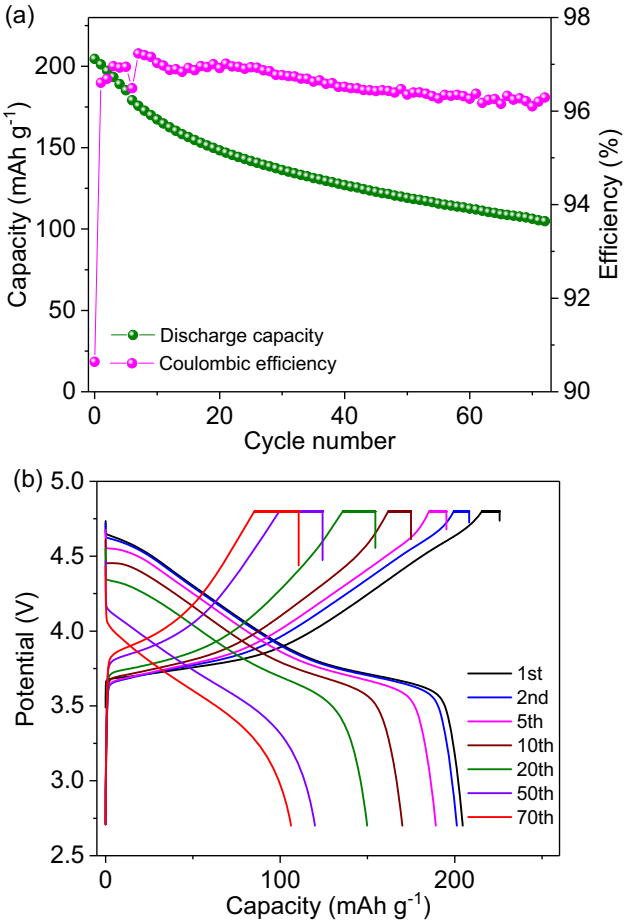

Figure 5. Electrochemical cycling performance and the corresponding charge-discharge curves of a Li/NCM111 cell between 2.7 and 4.8 V.

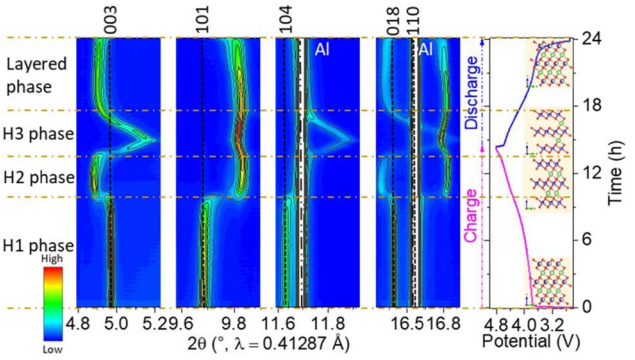

Figure 6. In situ SRD of NCM111 electrode: Contour plot of reflection evolution of 003, 101, 104, 018 and 110 during the first delithiation-lithiation.

move to higher 2-θ angles, indicating a solid solution reaction with an increasing *c* parameter and reduced *a* ($a = b$) parameter as for the layered hexagonal phase H1. In the voltage region from 4.2 to ~ 4.4 V, a new hexagonal phase H2 starts to form and grows at the expense of phase H1. The new phase H2 has the same layered structure as phase H1 but it possesses an expanded *c* parameter and a decreased *a* lattice parameter, as the number of Li ions is decreasing in the layered host structure. When the lithium ions are further extracted from NCM111 cathode, i.e. after charging to voltages higher than 4.6 V, the 003, 104, 018 reflections significantly move toward higher scattering angles and 101, 110 reflections shift to lower scattering angles simultaneously, implying a continuous phase transition from phase H2 to layered hexagonal phase H3. During lithiation (discharge), the changes of these reflections reverse directions but no pronounced biphasic region is found, implying a typical solid solution reaction mechanism for the layered phase.

Each in situ SRD pattern during first cycle was fitted using Rietveld refinement with the $R\bar{3}$m structure model, see Figure 7. The corresponding lattice parameters obtained are shown in Figure 8. From open-circuit voltage to 4.2 V, parameter *c* of phase H1 increases from 14.262(1) to 14.275(1) Å, and parameter *a* decreases from 2.865(1) to 2.862(1) Å. The expansion of the *c* value is supposed to be caused by the increased electrostatic repulsive force within the fcc oxygen lattice resulting from the decreased number of Li ions in the Li layer of NCM111. The contracting *a* parameter can be ascribed to the reducing radii of TM cations at higher valence states. The lattice parameters evolution of phase H2 are comparable with those of phase H1, corresponding to the voltage slope from 4.2 to 4.6 V. It should be noted that the expansion of lattice constant *c* and the contraction of *a* results in a higher *c*/*a* ratio of phase H2 (see Figure 8), indicating a better-defined layered hexagonal structure in phase H2 when compared with phase H1. Additionally, the splitting between 018 and 110 reflections becomes obvious, again suggesting that phase H2 has a highly layered property. With the voltage further increasing to 4.8 V, removal of more Li ions from the Li layer results in the formation of the layered hexagonal phase H3, as confirmed by the splitting of the 003 reflection in the diffraction patterns (see Figure 7d), and the turning point of the evolution of the lattice parameter of NCM111 electrode (Figure 8). Inspiringly, the I_{003}/I_{104} value of NCM111 cathode at a highly delithiated state (4.8 V) is approximately 1.73, which is very close to that of pristine electrode (~ 1.68), suggesting the nanodomain structure formation of the phase H3 rather than the production of a cubic rock-salt phase in NCM111 electrode. It is clear that the lattice parameter *c* shows a rapid decrease from 14.219(1) to 13.876(1) Å and parameter *a* slightly increases from 2.822(1) to 2.829(1) Å as a significant amount of lithium (higher than ~ 0.7 Li) is extracted from the layered structure. This phenomenon is probably attributed to the phase transformation from a layered phase H2 to phase H3 or cubic spinel nano-domains, which results from the oxygen release and the TM migration, leading to a reduction of the electrostatic repulsion between oxygen-oxygen layers along the *c*-axis and an expansion along the *a* (and *b*) axis. It also means that the *c*/*a* ratio decreases considerably during the deep-degree de-lithiation process. Specifically, the *c*/*a* ratio reaches a minimum value of 4.905(1) for voltages up to 4.8 V, which is within the experimental error very close to 4.899, the typical value for a cubic phase, revealing a poor hexagonal layered property for phase H3. This result is also in good accordance with the evolution of the 018/110 reflection pair, showing pronounced splitting at the beginning of charge but merge into a single reflection at the end of charge at 4.8 V. It should be mentioned that it is very difficult to distinguish between layered phase H3 and cubic spinel by synchrotron radiation diffraction. Therefore, the cubic spinel structure model was not utilized in the Rietveld refinement. During the lithiation (discharge), the lattice parameter *c* increases significantly and then decreases slightly, but it dose not reach the original value from before cycling. The difference in lattice constant *a*, *c* and *V* before and after the first cycle is 0.037(1) Å, 0.181(1) Å, and 1.324(1) Å^3, respectively, indicating an irreversible structural degradation of the NCM111 electrode for a high cutoff voltage of 4.8 V and hence resulting in a poor electrochemical performance as shown in Figure 5.

Finally, Raman spectroscopy was exploited to probe the local structure of NCM111 electrode at high state-of-charge (SOC) since this method is able to discriminate between layered and spinel phases. Figure 9a exhibits the Raman mapping of the NCM111 electrode after charging to at 4.8 V. The mapping image is the result of the Raman spectra collected within the area as shown in Figure 9a. The red, green and blue colors are consistent with the band intensity at 598 cm^{-1}, which is the strongest Raman peak of the layered structure.[32] Notably, the spectrum of region B displays an extra peak at 641 cm^{-1}, which

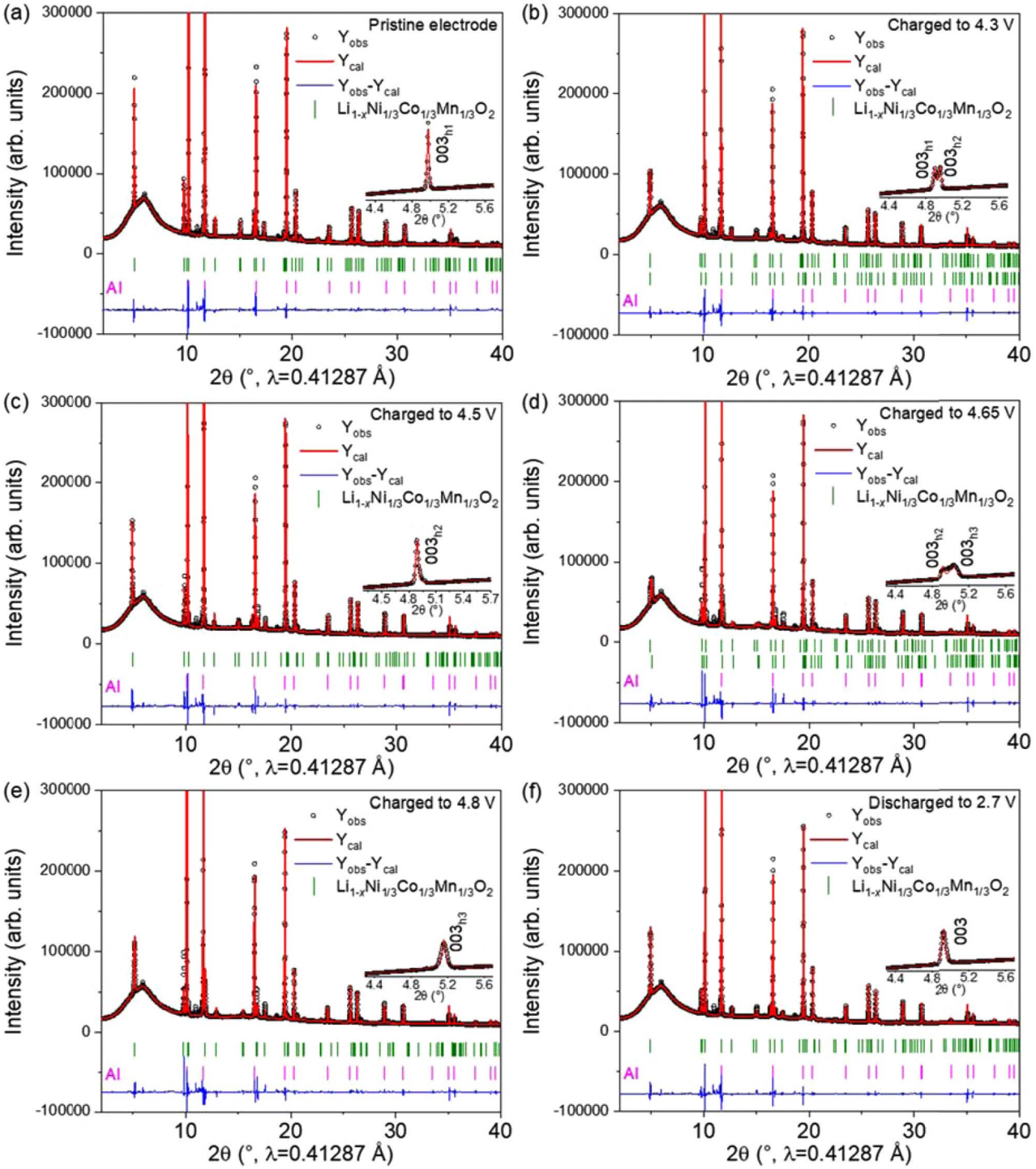

Figure 7. Rietveld refinement revealing the structural evolution of NCM111 electrode: (a) hexagonal phase H1 at open-circuit potential; (b) H1-H2 biphasic region at 4.3 V; (c) single phase H2 at 4.5 V; (d) H2-H3/cubic (not shown) biphasic region at 4.65 V; (e) layered phase H3 or cubic phase (not shown) at 4.8 V; and (f) layered hexagonal phase at 2.7 V.

is characteristic for a typical spinel phase (space group $Fd\bar{3}m$) due to its high symmetry,[33] revealing heterogeneity in NCM111 agglomerates on the micrometer-scale and oxygen loss upon a deep-degree de-lithiation to 4.8 V. Together with the results of in situ SRD, it can be concluded that the highly de-lithiated NCM111 cathode possesses the layered phase H3 in a nanodomain configuration together with small amounts of spinel phase. Recently, Liu et al. reported that the concurrent doping of La and Al stabilizes the structure and suppresses order-disorder phase transitions of layered $LiCoO_2$ during cycling at high-voltages of 4.5 V.[34] So the doping technique is suggested in order to improve the structural stability of NCM111 during high-voltage cycling through mitigating the collapse in the *c* direction.

Conclusions

$LiNi_{1/3}Co_{1/3}Mn_{1/3}O_2$ (NCM111) agglomerates were successfully synthesized by a hydroxide co-precipitation method followed by a high-temperature thermal treatment. A combination of SRD, NPD

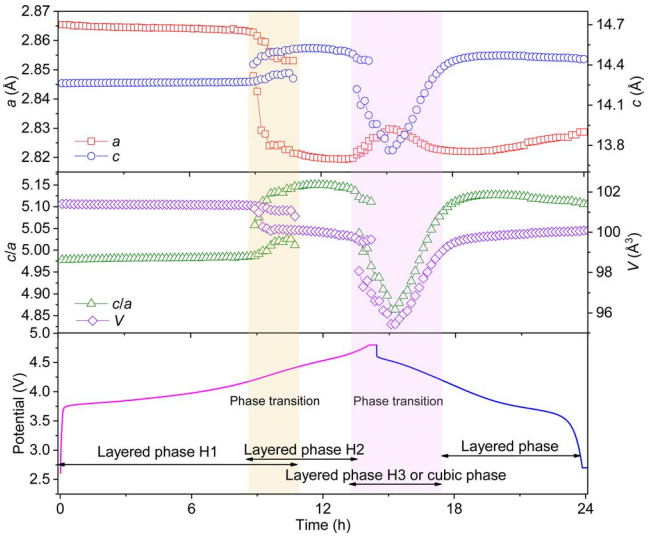

Figure 8. Lattice parameter changes of NCM111 cathode during the first charge-discharge process.

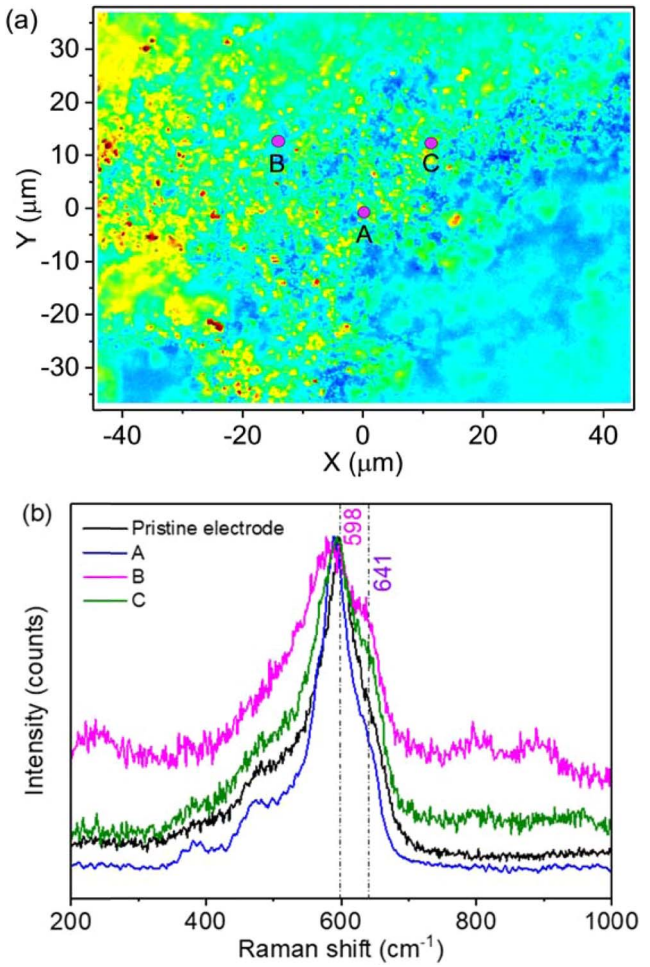

Figure 9. (a) Raman mapping image of NCM111 electrode charged at 4.8 V, and (b) Raman spectra of charged NCM111 electrode within the selected areas shown in (a) and the pristine NCM111 cathode.

and TEM confirms that NCM111 owns a well-defined layered hexagonal structure. Unfortunately, the NCM111 cathode in the lithium ion battery exhibits poor electrochemical performance in the voltage range from 2.7 to 4.8 V. Although no distinct plateau is observed from electrochemical curves, the fabricated NCM111 electrode experiences a phase transformation from layered hexagonal phase H1 to phase H2 and finally to phase H3 or cubic spinel phase upon deep de-lithiation to 4.8 V. The nanodomain formation of a layered phase H3 and/or a spinel phase causes the collapse of the layered host structure in the *c* direction, resulting in an irreversible structural transformation and thus capacity fading. Suppression of this collapse in the *c* direction is expected to be necessary in order to ensure good structural stability and a prolonged cyclability.

Acknowledgment

This work was supported by the Deutsche Forschungsgemeinschaft (DFG) under SFB 595 "Electrical Fatigue in Functional Materials" (project T3). The Bundesministerium für Bildung und Forschung (BMBF) supports Energy Research With Neutrons (ERWIN) with grant no. 05K16VK2. These experiments were performed at the MSPD beamline at ALBA Synchrotron with the collaboration of ALBA staff and CALIPSOplus (grant 730872) funding. The TEM characterization was performed at the Karlsruhe Nano Micro Facility, a Helmholtz research infrastructure operated at the KIT. W. H. received financial support from the China Scholarship Council (CSC). The authors gratefully acknowledge Margarete Offermann for helping with the material preparation, Udo Geckle for the SEM measurements, Liuda Mereacre for the Raman experiments. This work contributes to the research performed at CELEST (Center for Electrochemical Energy Storage Ulm-Karlsruhe).

ORCID

Weibo Hua https://orcid.org/0000-0001-5372-4422
Björn Schwarz https://orcid.org/0000-0002-9461-1448
Anatoliy Senyshyn https://orcid.org/0000-0002-1473-8992
Sylvio Indris https://orcid.org/0000-0002-5100-113X

References

1. M. Wagemaker, A. P. M. Kentgens, and F. M. Mulder, *Nature*, **418**, 397 (2002).
2. W. B. Hua, S. N. Wang, X. D. Guo, S. L. Chou, K. Yin, B. H. Zhong, and S. X. Dou, *Electrochim. Acta*, **186**, 253 (2015).
3. H. Liu, H. Liu, S. H. Lapidus, Y. S. Meng, P. J. Chupas, and K. W. Chapman, *J. Electrochem. Soc.*, **164**, A1802 (2017).
4. K. M. Shaju, G. V. Subba Rao, and B. V. R. Chowdari, *Electrochim. Acta*, **48**, 145 (2002).
5. Y. Fujii, H. Miura, N. Suzuki, T. Shoji, and N. Nakayama, *Solid State Ionics*, **178**, 849 (2007).
6. W. Hua, Z. Wu, M. Chen, M. Knapp, X. Guo, S. Indris, J. R. Binder, N. N. Bramnik, B. Zhong, H. Guo, S. Chou, Y.-M. Kang, and H. Ehrenberg, *J. Mater. Chem. A*, **5**, 25391 (2017).
7. W. B. Hua, X. D. Guo, Z. Zheng, Y. J. Wang, B. H. Zhong, B. Fang, J. Z. Wang, S. L. Chou, and H. Liu, *J. Power Sources*, **275**, 200 (2015).
8. X. Zhang, Z. Chen, B. Schwarz, F. Sigel, H. Ehrenberg, K. An, Z. Zhang, Q. Zhang, Y. Li, and J. Li, *Electrochim. Acta*, **227**, 152 (2017).
9. I. Belharouak, Y. K. Sun, J. Liu, and K. Amine, *J. Power Sources*, **123**, 247 (2003).
10. K. Luo, M. R. Roberts, R. Hao, N. Guerrini, D. M. Pickup, Y. S. Liu, K. Edström, J. Guo, A. V. Chadwick, L. C. Duda, and P. G. Bruce, *Nat. Chem.*, **8**, 684 (2016).
11. J. Kasnatscheew, U. Rodehorst, B. Streipert, S. Wiemers-Meyer, R. Jakelski, R. Wagner, I. C. Laskovic, and M. Winter, *J. Electrochem. Soc.*, **163**, A2943 (2016).
12. M. Evertz, F. Horsthemke, J. Kasnatscheew, M. Börner, M. Winter, and S. Nowak, *J. Power Sources*, **329**, 364 (2016).
13. W. Hua, Y. Wang, Y. Zhong, G. Wang, B. Zhong, B. Fang, X. Guo, S. Liao, and H. Wang, *Chin. J. Chem.*, **33**, 261 (2015).
14. J. Li, S. Xiong, Y. Liu, Z. Ju, and Y. Qian, *Nano Energy*, **2**, 1249 (2013).
15. D. Wang, I. Belharouak, L. H. Ortega, X. Zhang, R. Xu, D. Zhou, G. Zhou, and K. Amine, *J. Power Sources*, **274**, 451 (2015).
16. J. Li, R. Shunmugasundaram, R. Doig, and J. R. Dahn, *Chem. Mater.*, **28**, 162 (2016).
17. J. Shu, R. Ma, L. Shao, M. Shui, K. Wu, M. Lao, D. Wang, N. Long, and Y. Ren, *J. Power Sources*, **245**, 7 (2014).
18. L. Li, L. C. Wang, X. X. Zhang, M. Xie, F. Wu, and R. J. Chen, *ACS Appl. Mater. Interfaces*, **7**, 21939 (2015).

19. W. Hua, W. Liu, M. Chen, S. Indris, Z. Zheng, X. Guo, M. Bruns, T.-H. Wu, Y. Chen, B. Zhong, S. Chou, Y.-M. Kang, and H. Ehrenberg, *Electrochim. Acta*, **232**, 123 (2017).
20. W. Hua, J. Zhang, Z. Zheng, W. Liu, X. Peng, X. D. Guo, B. Zhong, Y. J. Wang, and X. Wang, *Dalt. Trans*, **43**, 14824 (2014).
21. J. K. Maichle, J. Ihringer, and W. Prandl, *J. Appl. Crystallogr.*, **21**, 22 (1988).
22. Z. Lu, D. D. MacNeil, and J. R. Dahn, *Electrochem. Solid-State Lett.*, **4**, A200 (2001).
23. M.-H. Lee, Y.-J. Kang, S.-T. Myung, and Y.-K. Sun, *Electrochim. Acta*, **50**, 939 (2004).
24. M. Sathiya, A. M. Abakumov, D. Foix, G. Rousse, K. Ramesha, M. Saubanère, M. L. Doublet, H. Vezin, C. P. Laisa, A. S. Prakash, D. Gonbeau, G. VanTendeloo, and J.-M. Tarascon, *Nat. Mater.*, **14**, 230 (2015).
25. X. Zhang, W. J. Jiang, A. Mauger, F. Gendron Qilu, and C. M. Julien, *J. Power Sources*, **195**, 1292 (2010).
26. T. Ohzuku, A. Ueda, and M. Nagayama, *J. Electrochem. Soc.*, **140**, 1862 (1993).
27. W. Luo, X. Li, and J. R. Dahn, *Chem. Mater.*, **22**, 5065 (2010).
28. A. Yano, S. Aoyama, M. Shikano, H. Sakaebe, K. Tatsumi, and Z. Ogumi, *J. Electrochem. Soc.*, **162**, A3137 (2015).
29. J. P. Baboo, H. Park, J. Song, S. Kim, J. Jo, D. T. Pham, V. Mathew, Z. Xiu, and J. Kim, *Electrochim. Acta*, **224**, 243 (2017).
30. S. Uchida, N. Zettsu, K. Hirata, K. Kami, and K. Teshima, *RSC Adv.*, **6**, 67514 (2016).
31. X. Zheng, T. Huang, Y. Pan, W. Wang, G. Fang, K. Ding, and M. Wu, *ACS Appl. Mater. Interfaces*, **9**, 18758 (2017).
32. M. L. Marcinek, J. W. Wilcox, M. M. Doeff, and R. M. Kostecki, *J. Electrochem. Soc.*, **156**, A48 (2009).
33. J. Yang, X. Han, X. Zhang, F. Cheng, and J. Chen, *Nano Res.*, **6**, 679 (2013).
34. Q. Liu, X. Su, D. Lei, Y. Qin, J. Wen, F. Guo, Y. A. Wu, Y. Rong, R. Kou, X. Xiao, F. Aguesse, J. Bareño, Y. Ren, W. Lu, and Y. Li, *Nat. Energy*, 1 (2018).